Journal of Materials Chemistry A

ROYAL SOCIETY OF CHEMISTRY

PAPER

View Article Online
View Journal | View Issue

Cite this: J. Mater. Chem. A, 2024, 12, 15666

Doping implications of Li solid state electrolyte $Li_7La_3Zr_2O_{12}$†

Kristoffer Eggestad, Sverre M. Selbach and Benjamin A. D. Williamson *

Received 4th March 2024
Accepted 26th May 2024

DOI: 10.1039/d4ta01487a

rsc.li/materials-a

Solid-state electrolytes, like $Li_7La_3Zr_2O_{12}$ (LLZO), can enable safer, more energy dense and longer lasting batteries. We investigate the effect of doping in LLZO with Al, Ga, Nb, Ta, and Y by hybrid density functional theory calculations and a full defect model. The site preferences of Al, Ga, Nb, and Ta result in donor defects that favour more Li vacancies and thus a more disordered Li substructure. This also implies stabilisation of the more ionic conducting cubic phase at the expense of the tetragonal, as seen experimentally. Furthermore, our calculations indicate that the effect of the dopants on the sintering process is even more important than the ability to induce more ionic charge carriers. Finally, differences in Li vacancy formation energies suggest a new possible explanation for the two orders of magnitude increase in ionic conductivity upon stabilising the cubic phase.

1 Introduction

Li-ion batteries are present in almost all portable electronic devices and play a crucial role in modern society. There is, however, a rising demand for safer batteries with both higher energy density and longer lifetime. One possibility is to replace the current liquid electrolyte with a solid-state electrolyte (SSE). In this way, one can theoretically increase the energy density with the use of Li metal anodes[1] by physically hindering Li dendrite formation and growth.[2] Additionally, the use of SSEs will result in safer batteries due to the removal of the highly flammable liquid electrolyte, thus facilitating a wider range of operating temperatures.[3] However, the implementation of SSEs has proven challenging as current materials suffering from low ionic conductivities,[4,5] poor air and water stability,[6,7] poor electrolyte–electrode interfaces,[8] as well as dendrite growth across grains and cracks, in spite of the solid electrolyte.[9,10] Good contact between the electrolyte and the electrodes is necessary to realise a well-functioning battery with long-term cyclability. Chemical expansion as well as different thermal expansion coefficients make good electrode–electrolyte interfaces very challenging to prepare and to maintain throughout operation.[8]

In 2003 a group of materials with the garnet structure were suggested as potential SSEs.[11] Early studies on garnet materials displayed high stability alongside Li-ion conductivities of about 10^{-6} S cm^{-1}. To date, arguably the most well studied garnet SSE is $Li_7La_3Zr_2O_{12}$ (LLZO) displaying relatively high Li-ion conductivities of $\sim 10^{-6} - 10^{-3}$ S cm^{-1} depending on doping, synthesis technique and environment, and the structural phase of LLZO.[12–17] At room temperature (RT), the structure is stable in its tetragonal form (space group: $I4_1/acd$), whilst at higher temperatures it undergoes a phase transition into the disordered cubic phase (space group: $Ia\bar{3}d$) which possesses ionic conductivities around two orders of magnitude higher than the tetragonal phase.[12,18]

The wide electrochemical stability window of LLZO allows it to benignly contact with Li metal anodes.[12,19,20] However, a very thin layer of tetragonal-like LLZO structure has been observed at the interface between cubic LLZO and Li metal[19,21] potentially resulting in a bottleneck to the Li-ion conductivity at the electrolyte–anode interface. Such a phenomenon means that it is important to understand Li transport and defects within both tetragonal LLZO as well as cubic LLZO.

In the first reported synthesis Murugan *et al.* made use of a conventional solid-state method with LiOH, La_2O_3, and ZrO_2 with a sintering temperature of 1230 °C.[12] Unfortunately, such a high sintering temperature results in substantial Li loss[22] and can furthermore lead to destabilisation of the LLZO structure and formation of the competing pyrochlore: $La_2Zr_2O_7$.[23] Undoped materials prepared by sol–gel synthesis has been shown to have approximately 3 times higher conductivity than solid-state prepared, most likely due to more homogenous and dense samples. However, LLZO prepared by the sol–gel method show lower thermal stability, due to larger grain size.[24] A further alternative is to use pulsed laser deposition (PLD) allowing for precise control of composition and stoichiometry, and can be used to prepare thin films of LLZO.[25,26]

One of the challenges concerning LLZO is the relatively poor ionic conductivity at grain boundaries,[27] the reasons for which are debated.[28,29] In general, grain boundaries in oxide electrolytes are known to reduce the overall ionic conductivity,[12,29]

Department of Materials Science and Engineering, NTNU Norwegian University of Science and Technology, Trondheim 7491, Norway. E-mail: benjamin.williamson@ntnu.no

† Electronic supplementary information (ESI) available. See DOI: https://doi.org/10.1039/d4ta01487a

although the opposite[30] can also be true for some materials. As a result, the sintering process of the electrolyte is important for reducing the grain boundary to bulk ratio. Grain boundaries in LLZO have also shown a susceptibility to Li dendrite formation and propagation. Additionally, good electrode–electrolyte contact is difficult to achieve, and easily forms cracks, leading to poor ionic conductivities as well as dendrite growth.[10]

The main difference between the cubic and the tetragonal LLZO structure is the Li substructure. In the tetragonal structure there are three fully occupied Li Wyckoff sites; Li_{8a}, Li_{16f}, Li_{32g}, a tetrahedral, an octahedral and a distorted octahedral site, respectively.[31] In the cubic structure there are only two different Wyckoff sites; Li_{24d}, Li_{96h}, a tetrahedral and a distorted octahedral site.[31] Both sites are partially occupied[32] and thus the Li substructure in the cubic structure is often described as disordered. Furthermore, a third Wyckoff site, Li_{48g}, is also often mentioned, but is an average position of a pair of Li_{96h} sites.[33] The tetragonal and the cubic structure are visualised together with their Li Wyckoff sites in Fig. 1 and ESI S1,† respectively.

Stabilising the cubic structure at RT is often achieved through aliovalent doping motivated by increasing the disorder on the Li substructure. Bernstein *et al.*[31] postulate that there is a critical amount of V_{Li} which results in an increased configurational entropy on the Li substructure, thus disfavouring an ordering of the Li sites and stabilising the cubic structure. The large increase in ionic conductivity is often attributed to the slightly shorter distances between the Li sites in the cubic structure and to the partial occupancy of these sites.[31] Several different dopants have been shown experimentally to enhance Li-ion conductivity in LLZO, however the mechanism of the resulting enhancement in conductivity is not well understood. Additionally, reported ionic conductivities are typically not easily comparable between studies due to differences in experimental setups.

The Li_{24d} site preference of Al in LLZO is well documented[34–36] and is also reported for Ga.[37,38] However, NMR studies found both Al and Ga ions to be equally distributed over the 24d and 96h sites.[39] NMR spectroscopy studies also indicate that Al substitutes both Zr and La sites at high doping concentrations.[40] Experiments with co-doping with both Al and Ga have been shown to stabilise the cubic phase and increase the ionic conductivity[39,41,42] with Ga often reported to give higher ionic conductivities,[43,44] however the reason for this is not well understood. In garnet materials, other phases with relatively low melting temperatures, such as $LiAlO_2$, Li_5AlO_4, and $LiGaO_2$, are often reported in the grain boundaries and are believed to aid grain growth and densification during sintering.[45,46]

Nb and Ta have also been shown to stabilise the cubic LLZO structure,[47,48] both preferring Zr sites,[49] thus acting as donor dopants and increasing the V'_{Li} concentration.

Y is commonly used as a sintering aid in LLZO[50] helping with densification, which in turn results in higher ionic conductivities.[15,51] Gai *et al.*[52] have shown that co-doping with Nb and Y gives good ionic conductivity and improved air stability. The effect of Y-doping on the stabilisation of the cubic phase has not been explicitly studied despite Y-doped cubic LLZO having been reported.[15] The site preference of Y and the resulting defects are also not clear, with Y_{Zr} and Y_{La} sites being reported in the literature.[15,51] Out of the common dopants, Y is the only dopant, which is predicted by Liu *et al.*[53] to result in a thermodynamically stable structure against Li metal anodes.

Here we use hybrid density functional theory (DFT) to investigate the role of Al, Ga, Nb, Ta, and Y doping in tetragonal LLZO. We calculate and compare defect formation energies, and investigate binding energies between dopants and charge carriers. Furthermore, we use calculated defect formation energies to predict changes in V'_{Li} concentrations resulting from the addition of the different dopants.

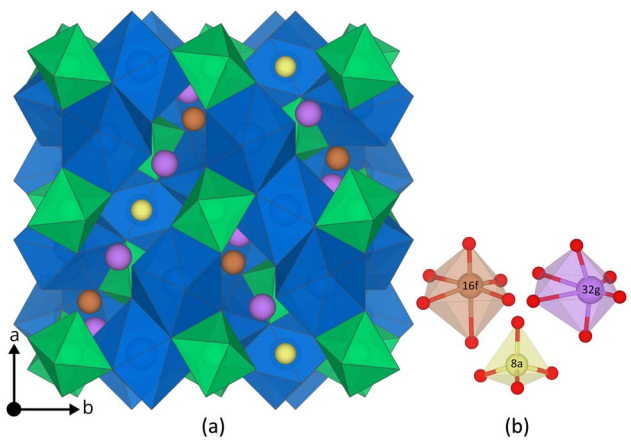

Fig. 1 (a) The tetragonal LLZO structure. La and Zr polyhedra are coloured in blue and green, respectively, O is omitted for clarity, and Li Wyckoff sites (16f = orange, 32g = purple, and 8a = yellow) are displayed in more detail in (b). The figure is made using the visualisation software VESTA.[72]

2 Computational methods

Density functional theory (DFT) calculations have been performed with the VASP[54–56] code to investigate the effect of Al, Ga, Nb, Ta and Y doping on the defect chemistry of tetragonal LLZO. Handling partial occupancies with DFT is computationally demanding as a large number of possible configurations needs to be evaluated and as such, no calculations were performed on the cubic LLZO structure. Additionally, the cubic structure is not the ground state structure and thus relaxing different configurations of the cubic structure can result in the cells transforming into the tetragonal structure as symmetry constraints must be turned off. The PBEsol[57] (Perdew–Burke–Ernzerhof revised for solids) functional was used for the initial screening of dominant intrinsic defects to reduce computational cost which were then treated with the Heyd–Scuseria–Ernzerhof screened hybrid functional (HSE), with mixing parameter $\alpha = 0.25$ and screening parameter $\omega = 0.11$ bohr^{-1} (HSE06).[58] Hybrid functionals have consistently been shown to offer a greater agreement with experiment, particularly with respect to defect chemistry.[59–61] All defects cells (96-atom unit cell) and their respective charge states were subjected to a geometry relaxation, keeping the cell parameters fixed, using a plane wave cutoff energy of 600 eV and a Monhorst-Pack *k*-

point of 2 × 2 × 2. The geometry was optimised until the forces on the ions were below 0.01 eV Å^{-1}. Li ($1s^2$, $2s^1$), La ($4s^2$, $4p^6$, $5s^2$, $5d^1$), Zr ($3s^2$, $3p^6$, $4s^2$, $4d^2$), O ($2s^2$, $2p^4$), Al ($3s^2$, $3p^1$), Ga ($3s^2$, $3d^{10}$, $4p^1$), Nb ($3s^2$, $3p^6$, $4s^2$, $4d^3$), Ta ($4p^6$, $5s^2$, $5d^3$), Y ($3s^2$, $3p^6$, $4s^2$, $4d^1$) were treated as valence electrons, and the interactions between valence electrons and cores were described by the projector-augmented wave method (PAW).[62] Inequivalent interstitial sites were determined using a Voronoi tessellation approach as implemented within the pymatgen package.[63]

2.1 Thermodynamic transition levels

Defect formation energies were calculated using.[64]

$$\Delta H_F(D,q) = E_D(q) - E_H + \sum_i n_i(E_i + \mu_i) + q\left(E_F + E_{vbm} + E_{corr}^{pot}\right) + E_{corr}^{IC} \quad (1)$$

where q is the charge of the defect D, $E_D(q)$ is the energy of the defect cell, E_H is the energy of the host cell, i is the elements added to or removed from the host cell, n_i is the number of element i removed from the cell, E_i is the reference energy of element i, μ_i is the chemical potential of element i, E_F is the Fermi level, and E_{VBM} is the energy of the valence band maximum (VBM). E_{corr}^{pot} is the potential alignment correction aligning the defect potential to that of the bulk and E_{corr}^{IC} is the image charge correction calculated within the formalism developed by Lany and Zunger[65] and adapted for non-cubic cells by Murphy and Hine.[66]

2.2 Chemical potential limits

The thermodynamic stability region at the athermal limit of tetragonal LLZO was found by calculating possible competing phases. All structures were first geometrically optimised using the PBEsol functional to the same convergence criterion as bulk LLZO. Individual k-points and formation enthalpies for each phase are provided in ESI Tables S3–S8.† Thereafter, the Chemical Potential Limits Analysis Program (CPLAP)[67] was used to determine the thermodynamic stability region and thus the constrained chemical potential limits for LLZO. The phases that make up the boundaries of the stability region were then subjected to a geometry optimisation using HSE06 and new enthalpies of formation were calculated the details or which are given in ESI Table S9.†

2.2.1. Chemical potentials at experimental conditions. The chemical potentials were chosen to best resemble typical experimental synthesis conditions: sintering at 1200 °C in air, the latter environment has been shown to result in the optimum ionic conductivities in LLZO.[68] The chemical potential of oxygen in this environment can be calculated ($\mu_O = \sim -1.90$ eV) using thermochemical tables[69] within the formalism outlined by Reuter and Scheffler:[70]

$$\mu_O(T,p) = \mu_O(T,p^\circ) + \frac{1}{2}k_B T \ln\left(\frac{p}{p^\circ}\right) \quad (2)$$

$$\mu_O(T,p^\circ) = \frac{1}{2}[H(T,p^\circ,O_2) - H(0\ K,p^\circ,O_2)] + \frac{1}{2}[S(T,p^\circ,O_2) - S(0\ K,p^\circ,O_2)] \quad (3)$$

where H, S, p, T and k_B are the enthalpy, entropy, partial pressure of oxygen, temperature, and Boltzmann's constant, respectively. The chemical potentials for the constituent elements follow from the stability region displayed in ESI Fig. S2.†

2.3 Equilibrium defect concentrations

The equilibrium defect concentration for a defect D with charge q is given by:

$$c(D,q) = N_D g_{D,q} \exp\frac{-\Delta H_f(D,q)}{k_B T} \quad (4)$$

where N_D is the density of possible sites for defect D, $g_{D,q}$ is the degeneracy of the defect state, k_B is Boltzmann's constant, and T is temperature.[59] The formation energy of charge state q is dependent on the Fermi energy (E_F) which can itself be determined self consistently within the charge neutrality condition:

$$\rho(E_F) = \sum_{D_q} q \cdot c(D,q) + p_0 - n_0 = 0 \quad (5)$$

where electron (n_0) and hole (p_0) concentrations are functions of the Fermi energy (E_F) and the electronic density of states for the bulk material ($g(E)$):

$$n_0 = \int_{E_{CBM}}^{\infty} \frac{1}{\exp\left(\frac{E - E_F}{k_B T}\right) + 1} g(E)\mathrm{d}E \quad (6)$$

$$p_0 = \int_{-\infty}^{E_{VBM}} \left(1 - \frac{1}{\exp\left(\frac{E - E_F}{k_B T}\right) + 1}\right) g(E)\mathrm{d}E \quad (7)$$

SC-FERMI by Buckeridge[71] was used to calculate the self consistent Fermi level within this work. Defect concentrations and Fermi levels are determined for a range of temperatures from the sintering temperature of 1200 °C to RT.

3 Results and discussion

The DFT optimised tetragonal LLZO structure with its three Li Wyckoff sites: 8a, 16f, and 32g are displayed in Fig. 1.

The calculated lattice parameters, displayed in ESI Table S1† are in excellent agreement with reported experimental XRD data (within ~0.6%).[73,74] The calculated band gap of 5.92 eV is also in good agreement with experiments showing an optical band gap of ~6 eV.[75] Other DFT simulations using HSE06 show a similar band gap to our results[76] and hybrid functionals such as HSE06 are known to accurately reproduce the electronic structure of semiconductors and insulators.[61] The PBEsol bandgap is calculated to be ~4 eV in line with PBEsol's typical underestimation of the bandgap due to the well known self-interaction error.[77,78]

3.1 Intrinsic defects

The thermodynamic transition levels for the dominant intrinsic defects (a) and dopant species (b–f) calculated using the HSE06

functional at chemical potentials representative of the sintering temperature in air at 1200 °C are given in Fig. 2. Based on the study by Squires *et al.*[76] and an initial screening using PBEsol (transition levels given in ESI Fig. S4†), it can be seen that the formation energies of the Li Frenkel defect V'_{Li} and $Li_i^{\cdot}$, eqn (8), are >1 eV lower than all other intrinsic defects at the Fermi level (E_F), with the exception of $V_O^{\cdot\cdot}$ and O''_i at very O poor or rich conditions respectively. As both Li and O defects dominate the defect chemistry in LLZO these were calculated using HSE06 in order to determine the effects of extrinsic doping. Our initial screening and calculations performed by Squires *et al.*[76] show a very small difference in formation energy (<0.05 eV) between tetrahedrally and octahedrally coordinated V'_{Li}. In spite of these results, our calculations using HSE06 result in notably larger differences in the formation energies of these defects. $V'_{Li}(32g)$ and $V'_{Li}(8a)$ possess very similar formation energies of ~0.47 and ~0.55 eV, respectively. However, the formation energy of $V'_{Li}(16f)$ is ~0.76 eV, which is 0.29 eV higher than the formation energy of $V'_{Li}(32g)$ thus we expect a strong ordering of the V'_{Li} defects at the sintering temperature. It can be proposed that this will result in larger migration barriers to and from the 16f sites than between the 8a and 32g sites. If one were to assume an increase in the migration barrier of ~0.2 eV, (similar to $\Delta H_f[V'_{Li}(16g)] - \Delta H_f[V'_{Li}(8a)]$) a reduced jump probability at RT from Boltzmann distribution of almost four orders of magnitude would be expected resulting in a drastically reduced ionic conductivity. More likely, however, Li ions will instead favour an alternative path without the 16f sites (8a ↔ 32g ↔ 32g ↔ 8a) and slightly longer jumps, thus also likely slightly larger migration barriers. This path is displayed in ESI Fig. S3.†

In the cubic LLZO structure, however, there are only two different Li sites: 24d and 96h which are similar in symmetry to the 8a and 32g sites in the tetragonal structure, respectively. Both the 8a and 24d sites are tetrahedrally coordinated, while the 32g and 96h sites are octahedrally coordinated. Furthermore, the 16f sites are slightly less distorted than the 32g and the 96h sites thus it is reasonable to argue that the 16f sites disappear when the cubic structure is formed and thus the removal of the 16f sites could explain the large difference in ionic conductivity between the tetragonal and cubic LLZO structure.

$$Li_{Li}^{x} + V_i^{x} \rightarrow V'_{Li} + Li_i^{\cdot} \quad (8)$$

3.2 Extrinsic defects

3.2.1. Al and Ga doping. Both dopants show very similar results preferring Li_{8a} substitution at the E_F with formation energies of ~0.62 eV and ~1.66 eV for Al and Ga respectively (Fig. 2(b) and (c)). The $Al(Ga)'_{Zr}$ defects have the second lowest

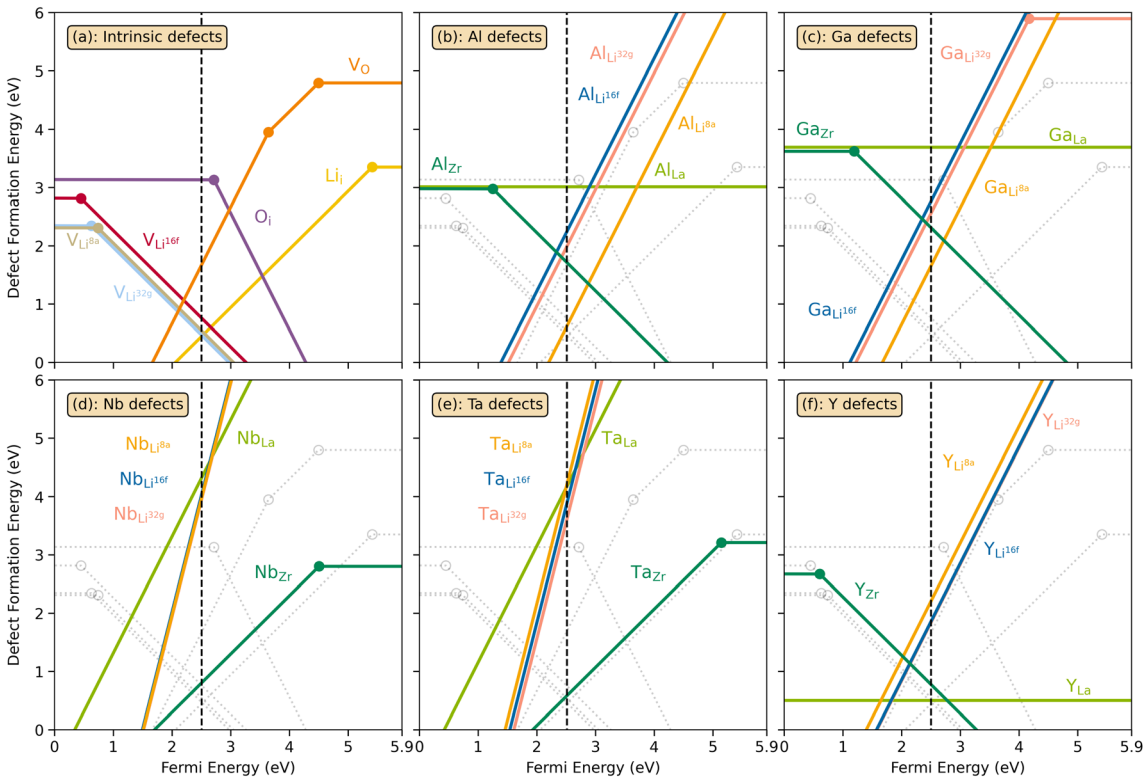

Fig. 2 Transition level diagrams for the formation energies of intrinsic defects (a) and selected dopants: Al (b), Ga (c), Nb (d), Ta (e) and Y (f). In each panel, the Fermi energy ranges from the valence band maximum (VBM) at 0 eV to the conduction band minimum (CBM) at ~5.9 eV. The chemical potentials, used for the calculated formation energies, were chosen to resemble sintering in air at 1200 °C and are displayed in ESI Fig. S2.† The black dashed vertical lines display the self-consistent Fermi level. Intrinsic defects are also displayed together with dopants as grey, transparent lines for clarity. Transition level diagrams for oxygen poor and oxygen rich environments are displayed in ESI Fig. S5 and S6.†

formation energies of ~1.72 eV (~2.31 eV) followed by $Al(Ga)^{\cdot\cdot}_{Li^{32g}}$ and $Al(Ga)^{\cdot\cdot}_{Li^{16f}}$ and lastly $Al(Ga)^{x}_{La}$ with formation energies of ~1.99 eV (~2.56 eV), ~2.25 eV (~2.77 eV), and ~3.01 eV (~3.69 eV) respectively. As both Al and Ga prefer Li sites, these dopants will be charge compensated mainly by the formation of V'_{Li}, see eqn (9). All Ga defects have formation energies 0.5–1 eV higher than the corresponding Al defects at the E_F, indicating much lower solubility than Al.

$$(Al/Ga)_2O_3 + 6Li^{x}_{Li} \rightarrow 2(Al/Ga)^{\cdot\cdot}_{Li} + 4V'_{Li} + 3Li_2O \quad (9)$$

Considering the ionic radii of 4 and 6 coordinated Al (0.39 Å, 0.535 Å) and Ga (0.47 Å, 0.62 Å) ions, a preference for the smallest sites, $Li_{8a/24d}$ (0.59 Å), is expected. However, despite what is reported on the site preference of Al and Ga ions in cubic LLZO,[34–38] the low formation energy for $Al(Ga)'_{Zr}$ is likely due to the small charge difference between the Al(Ga) and Zr ions. Considering the similarity between the Zr sites in the tetragonal and the cubic structure, we do not expect the formation energies of dopants at Zr sites to be notably different in the cubic structure. However, the same argument cannot be made for the Li sites, and therefore, the formation energies of dopants at Li sites in the cubic structure could be slightly different to what is presented in Fig. 2. There exists a high degree of ambiguity on the site preference of Al and Ga in cubic LLZO in the reported literature;[34–40] our results suggest a preference for the Li_{24d} sites, but do not discount the possibility of Al or Ga being located on Zr or Li_{96h} sites.

3.2.2. Y doping. It is evident from Fig. 2(f) that Y_{La} is dominant at E_F (ΔH_f = ~0.50 eV). This is reasonable considering the +3 charge of both ions in addition to the large ionic radii of both La and Y ions of 1.16 Å and 1.019 Å, respectively. As a charge neutral defect, Y_{La} will not require charge compensation and will only result in more cation disorder in the structure. More surprising is the low formation energy of ~0.78 eV of Y'_{Zr} at E_F. Y'_{Zr} enhances $Li^{\cdot}_{i}$ concentration as charge compensation, eqn (10).

$$Y_2O_3 + 2Zr^{x}_{Zr} + 2Li_2O + 2V^{x}_{i} \rightarrow 2Y'_{Zr} + 2Li^{\cdot}_{i} + 2ZrO_2 \quad (10)$$

3.2.3. Nb and Ta doping. Nb and Ta show an almost exclusive preference for Zr sites, Fig. 2(d) and (e), with formation energies of ~0.80 eV and ~0.59 eV, respectively and is in agreement with previous DFT studies.[49] $Nb(Ta)^{\cdot\cdot}_{La}$ possess formation energies ~3.5 eV higher than $Nb(Ta)^{\cdot}_{Zr}$ at E_F. The formation energy for $Nb^{\cdot}_{Zr}$ is about 0.2 eV higher than $Ta^{\cdot}_{Zr}$ implying a higher solubility of Ta than Nb in LLZO. Similar to Al and Ga, Nb and Ta will be charge compensated by the formation of additional V'_{Li}, eqn (11).

$$(Nb/Ta)_2O_5 + 2Zr^{x}_{Zr} + 2Li^{x}_{Li} \rightarrow 2(Nb/Ta)^{\cdot}_{Zr} + 2V'_{Li} + Li_2O + 2ZrO_2 \quad (11)$$

3.3 Electronic conductivity

Electrical conductivity (σ_e) in LLZO which has been linked to dendrite formation and growth;[79,80] thus a low σ_e is essential for longterm cyclability.[81] The electronic conductivity of tetragonal LLZO has also been investigated by first principles calculations by Squires *et al.*[82] wherein it is suggested that the bulk electronic conductivity of the structure is too low for governing dendrite growth and attributes the dendrite growth to surface and defect contributions. Our calculations show that in doped LLZO, E_F is trapped mid gap (~2.5 eV above the VBM) and each transition level of the aliovalent dopants occurs far from the band edges (tabulated in ESI Table S10†) thus no increase in conductivity is expected. Additionally, donor defects, such as $Al(Ga)^{\cdot\cdot}_{Li}$ and $Nb(Ta)^{\cdot}_{Zr}$, are compensated for by V'_{Li}, while acceptor defects, such as Y'_{Zr}, are compensated by $Li^{\cdot}_{i}$.

3.4 Defect concentrations

Li ions are highly mobile in LLZO even at very low temperatures, which is obviously also a prerequisite for its application as a solid-state electrolyte.[36] Two implications of this mobility is that, firstly, after sintering, all Li Frenkel pairs that emerge at elevated temperatures will relax back to the equilibrium RT concentration upon cooling. Secondly, when LLZO as an electrolyte layer is in electrical contact with a Li reservoir, like *e.g.* a Li metal anode, the Li concentration in LLZO will adjust according to the concentration of aliovalent dopants in the structure, regardless of possible Li loss during high-temperature synthesis and processing. In contrast with highly mobile Li, cation dopants are expected to be highly immobile due to their higher formal charge, low polarizability and general refractoryness of LLZO as a host crystal. Hence, the concentration of dopants is expected to freeze-in at elevated specific temperatures, causing non-equilibrium defect concentrations at lower temperatures. This situation has been described as broken ergodicity by Grande *et al.*[83] and the freezing-in of point defect populations is well-known in solid state ionics.[84]

In the following we discuss the experimentally important distinction between synthesis methods were the final cation stoichiometry (with the exception of Li) of the sample is constrained to the nominal stoichiometry of the precursor materials, and the situation where the final sample of interest can freely exchange dopants with the surroundings. Examples of the former situation are solid-state and sol–gel synthesis where all reactants contribute to the final sample material, thus maintaining the nominal stoichiometry. The latter situation applies to *e.g.* thin film deposition methods like pulsed lased deposition (PLD) or sputtering where there is not necessarily stochiometric transfer from target to film, and where there can be substantial segregation to the film edges, which are usually not investigated. Single crystal growth from melt and hydrothermal crystallization are also methods where the nominal composition of the reactants are not necessarily reflected by the true composition of the final material.

We first discuss the situation with constrained dopant stoichiometry. Typical nominal dopant concentrations in LLZO are 0.25 dopant per formula unit.[15,43,44,47,48] Assuming that all dopants are incorporated into the LLZO structure, this results in expected V'_{Li} concentrations of ~0.5 and ~0.25 per formula unit for Al/Ga and Nb/Ta, respectively, dashed lines in Fig. 3. This is typically what is assumed as the response to the addition of

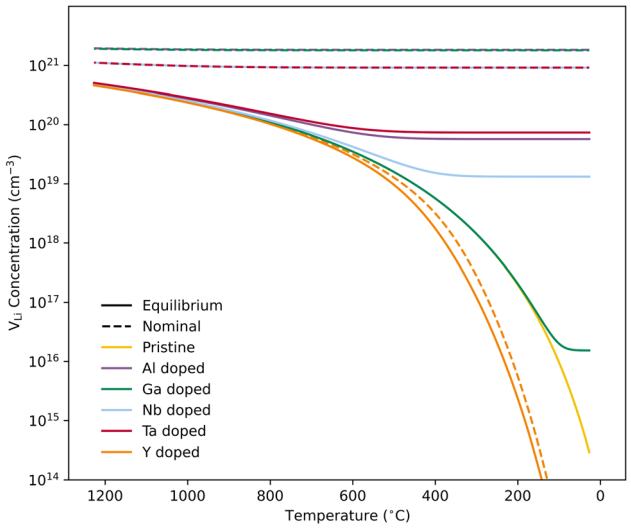

Fig. 3 V_{Li} concentration as a function of temperature with dopants related defects frozen-in at a sintering temperature of 1200 °C. Solid lines display calculated equilibrium V_{Li} concentrations, while dashed lines depict the V_{Li} concentration resulting from a nominal doping concentration of 0.25 per formula unit. A concentration of 10^{21} cm^{-3} is equivalent to ~0.27 per formula unit of $Li_7La_3Zr_2O_{12}$. The different lines correspond to the V_{Li} concentrations resulting from the different dopants.

dopants when making LLZO by solid-state and sol–gel syntheses. However, as indicated by the differences in the defect formation energies, some dopants are less energetically favoured than others, and thus may result in the formation of secondary phases or segregation towards grain boundaries or surfaces. Strain fields associated with grain boundaries are known to often reduce defect formation energies,[85] and lead to defects accumulation at or close to grain boundaries. Secondary phases at grain boundaries may be difficult to detect, but may still strongly affect the sintering properties, density and electrical properties of polycrystals.

Equilibrium dopant concentrations, Table 1, and resulting V'_{Li} concentrations, solid lines in Fig. 3, have been calculated to better address the solubility of the different dopants as well as dopant concentrations from open system synthesis methods. These concentrations have been estimated from athermal defect formation energies at the dilute limit with the assumption of equilibrium, meaning that elements can freely be added to or removed from the system. Except for Y, typical dopant concentrations are >10 times higher than the equilibrium concentrations calculated herein. In for example solid state synthesis, only volatile elements such as Li can disappear from the system, and thus lower equilibrium concentrations than nominal concentrations imply that there is a driving force for the formation of secondary phases.

Table 1 Typical nominal dopant concentrations and calculated equilibrium dopant concentrations given per formula unit of $Li_7La_3Zr_2O_{12}$

Dopant	Nominal (p.f.u.)	Equilibrium (p.f.u.)
Al	0.25	7.8×10^{-3}
Ga	0.25	2.1×10^{-6}
Nb	0.25	3.6×10^{-3}
Ta	0.25	2.0×10^{-2}
Y	0.25	5.9×10^{-1}

As equilibrium concentrations give an indication of the solubility of a specific dopant, out predicted value for Ga is several orders of magnitude lower than the other dopants, and doping with Ga is known to result in the formation of secondary phases.[46] Moreover, it has been reported by Schwab *et al.*[86] that 0.20 Ga per formula unit exceed the solubility limit of Ga in LLZO, and in their study, the amount of the secondary phases formed could not be detected by XRD. Furthermore, if we assume that all Ga added in this experiment result in the formation of $LiGaO_2$, the resulting volume fraction is ~3%, relatively close to the detection limit of regular XRDs. Therefore, the formation of relatively small amounts of secondary phases can easily be missed.

Fig. 3 shows how the V'_{Li} concentration changes as a function of cooling temperature for the pristine structure and different doping regimes, where the dopant concentrations are frozen-in at the sintering temperature. The dashed lines describe $[V'_{Li}]$ resulting from a nominal dopant concentration of 0.25 per formula unit and the assumption that all added dopants will be incorporated into the structure. The solid lines show $[V'_{Li}]$ resulting from equilibrium dopant concentrations. Regardless of the synthesis technique, dopants incorporated into the structure require charge compensation and will stabilise additional defects. Therefore, a dopant's "success" is highly dependent on both the quantity of dopant incorporated into the structure during sintering as well as the temperature at which its defects freezes-in. At what temperature the different dopants freezes-in is highly complex and has not been investigated in our work.

From our analysis, it is clear that all dopants, with the exception of Y, result in a drastic increase in the V'_{Li} concentration at RT. Ta-doping results in the largest estimated equilibrium $[V'_{Li}]$ at RT of 7.4×10^{19} cm^{-3} corresponding to ~0.02 defects per formula unit. The $[Ta^{\cdot}_{Zr}]$ frozen in at the sintering temperature is also 7.4×10^{19} thus it can be assumed that this is solely responsible for the increased $[V'_{Li}]$. Low formation energies of Y^{x}_{La} and Y'_{Zr} result in a higher equilibrium concentration than the nominal dopant concentration and hence the nominal dopant concentration showing less destabilisation of V'_{Li}.

Furthermore, it is often assumed that the added dopants only will reside on the lowest energy sites. This, however, is not true and is especially important to keep in mind when investigating dopants that result in defects with relatively high and similar formation energies at the Fermi level such as Ga:LLZO. There will be a Boltzmann distribution over all available lattice sites, and for Ga, this means that the dopants will mainly be located at Li and Zr sites, but also at La sites. This type of non-convergent disordering of cations has for instance been studied in spinels,[87,88] complex oxide $LaSr_{2-x}Ca_xCu_2GaO_7$ [89] and more recently in tetragonal tungsten bronzes.[90]

3.5 Binding energies

Binding energies between dopants and V'_{Li} give an indication of whether or not a dopant acts as a trapping point. Substantial binding energies could in turn result in reduced Li-ion mobility, and thus a reduced ionic conductivity. The binding energies displayed in Table 2 were calculated by subtracting the energy of a cell with a defect pair, where the defect related to a dopant is located close to (~3 Å) a V'_{Li}, from the energy of a cell, where they are located far away (~6 Å) from each other. Neutral cells ($q = 0$) were used for all calculations. The shortest distance between two Li_{8a} sites is ~6 Å, and therefore there are no calculated binding energies for $Al(Ga)_{Li^{8a}}$ with $V'_{Li^{8a}}$. This is also true for the Li_{16f} sites. The Y defects show the largest binding energies, closely followed by Ga. Both Nb and Ta show very small binding energies, indicating only weak trapping. A couple of the defect pairs show negative binding energies which means that the V'_{Li} is repelled by the dopant. At RT $k_BT \sim 0.025$ eV, and thus defect pairs with binding energies lower than 0.025 eV will not be noticeably affected by this barrier. However, small binding energies can contribute to a slight increase in migration barriers.

Neither Nb nor Ta are located on the Li substructure, and thus do not give strong V'_{Li} trapping, and have very low formation energies. However, both Al and Ga are reported with similar ionic conductivities despite being located on the Li substructure, and showing relatively high binding energies. Doping with Al, Ga, Nb or Ta increases disorder within the structure, in particular on the Li substructure, and therefore helps stabilise the cubic phase. We can therefore conclude that the stabilisation of the cubic structure is the main contribution to the high ionic conductivity and that the differences in the V'_{Li} concentrations are less important. Such a conclusion is in good agreement with the work carried out by Allen *et al.*[91] wherein they showed that codoping Ta-stabilised cubic LLZO with Al and Ga resulted in a reduction in the ionic conductivity from the monodoped Ta:LLZO (cubic phase), furthermore indicating that Al and Ga doping into the Li substructure disrupts Li-ion mobility. In addition, significant binding energies between Al/Ga and V'_{Li} suggest increased migration barriers, which supports the deactivation of Li-ion diffusion around Al and Ga ions observed in molecular dynamics simulations performed by García Daza *et al.*[92] Moreover, NMR studies by Posch *et al.*[93] also suggest enlarged migration barriers around Al ions. It is also important to note that not only migration energy barriers, as emphasized here, are important to the ionic conductivity, but also Arrhenius prefactors, as found in NMR studies of LLZO doped with Mo and Ta.[94,95]

Table 2 Binding energies between different V_{Li} and dopants given in eV. The missing values arises due to some sites not existing close to each other in the structure. Positive values describe attraction while negative values describe repulsion

	$V_{Li^{8a}}$	$V_{Li^{16f}}$	$V_{Li^{32g}}$
$Al_{Li^{8a}}$	—	—	0.060
$Ga_{Li^{8a}}$	—	—	0.183
Nb_{Zr}	0.013	0.016	−0.006
Ta_{Zr}	0.003	0.013	−0.016
Y_{Zr}	0.144	0.221	0.063
Y_{La}	0.213	−0.033	−0.088

3.6 Solid solubility, grain boundaries and sintering

Ga-doped LLZO is commonly reported with a higher ionic conductivities than the Al-doped variations. Our results, showing lower formation energies for Al defects, indicate that Al should be easier to incorporate into the structure, thus stabilising more V'_{Li} and increasing the number of charge carriers. However, this enhanced incorporation of Al in the structure will, in addition to increase the V'_{Li} concentration, result in more disruption of the Li diffusion paths than Ga. Furthermore, Al and Ga are known to segregate towards the grain boundaries forming competing phases with relatively low melting temperatures which beneficially act as sintering aids.[45,46] In so, Al and Ga crucially affect the poor grain boundary conductivity in polycrystalline LLZO. Based on Ga substitutional defects being less energetically favourable than Al defects in the structure, and thus Ga is expected to show a lower solid solubility, we expect this effect to be greater in Ga doped structures. The effect of Al and Ga acting as a sintering aid is likely a part of the explanation for why the reported ionic conductivities of both Al and Ga doped LLZO are similar to the Nb and Ta doped structures.

4 Conclusion

In summary, our calculations performed on the tetragonal LLZO polymorph are in agreement with published experimental work on the cubic polymorph. This implies that our results on the tetragonal phase are good indications of what to expect of the cubic. We suggest the disappearance of the Li_{16f} sites as a possible explanation for the large difference in ionic conductivity between the tetragonal and cubic polymorphs. Doping with Y does not result in an increased V'_{Li} concentration. Doping with Al, Ga, Nb, or Ta will increase the V'_{Li} concentration and increase disorder on the Li substructure, thus stabilising the cubic LLZO structure. Al and Ga are located on tetrahedrally coordinated Li sites and will as a result block Li paths and disrupt Li ion mobility. Doping LLZO with Ga has been shown experimentally to give the best ionic conductivities, but our calculations show that doping with Ga will result in some trapping and less stabilisation of V'_{Li} than the other donor defects. Therefore, we suggest that the effect of dopants on the sintering process is the most important property of the dopant after the ability to stabilise the cubic LLZO structure.

Author contributions

KE performed all the calculations and analysis related to this work with supervision from BADW. SMS contributed to the reviewing, editing and supervision of the work. All authors contributed to the review and editing of the final manuscript and have given approval to the final version of the manuscript.

Conflicts of interest

There are no conflicts of interest in this work.

Acknowledgements

Computational resources were provided by UNINETT Sigma2 through Project NN9264K. Support for this project was provided from the Research Council of Norway (Project Numbers 287890, 302506, 301954).

Notes and references

1 Y. Shen, Y. Zhang, S. Han, J. Wang, Z. Peng and L. Chen, *Joule*, 2018, **2**, 1674–1689.
2 K. B. Hatzell, X. C. Chen, C. L. Cobb, N. P. Dasgupta, M. B. Dixit, L. E. Marbella, M. T. McDowell, P. P. Mukherjee, A. Verma, V. Viswanathan, A. S. Westover and W. G. Zeier, *ACS Energy Lett.*, 2020, **5**, 922–934.
3 D. Aurbach, Y. Talyosef, B. Markovsky, E. Markevich, E. Zinigrad, L. Asraf, J. S. Gnanaraj and H.-J. Kim, *Electrochim. Acta*, 2004, **50**, 247–254.
4 J. G. Kim, B. Son, S. Mukherjee, N. Schuppert, A. Bates, O. Kwon, M. J. Choi, H. Y. Chung and S. Park, *J. Power Sources*, 2015, **282**, 299–322.
5 M.-J. Uddin and S.-J. Cho, *Sustainable Energy Fuels*, 2018, **2**, 1458–1462.
6 G. Sahu, Z. Lin, J. Li, Z. Liu, N. Dudney and C. Liang, *Energy Environ. Sci.*, 2014, **7**, 1053–1058.
7 Q. Zhao, S. Stalin, C.-Z. Zhao and L. A. Archer, *Nat. Rev. Mater.*, 2020, **5**, 229–252.
8 T. Famprikis, P. Canepa, J. A. Dawson, M. S. Islam and C. Masquelier, *Nat. Mater.*, 2019, **18**, 1278–1291.
9 C. Monroe and J. Newman, *J. Electrochem. Soc.*, 2005, **152**, A396.
10 C. Zhang, Q. Hu, Y. Shen and W. Liu, *Adv. Energy Sustainability Res.*, 2022, **3**, 2100203.
11 V. Thangadurai, H. Kaack and W. J. F. Weppner, *J. Am. Ceram. Soc.*, 2003, **86**, 437–440.
12 R. Murugan, V. Thangadurai and W. Weppner, *Angew. Chem., Int. Ed.*, 2007, **46**, 7778–7781.
13 C. Li, Y. Liu, J. He and K. S. Brinkman, *J. Alloys Compd.*, 2017, **695**, 3744–3752.
14 D. Rettenwander, G. Redhammer, F. Preishuber-Pflügl, L. Cheng, L. Miara, R. Wagner, A. Welzl, E. Suard, M. M. Doeff, M. Wilkening, J. Fleig and G. Amthauer, *Chem. Mater.*, 2016, **28**, 2384–2392.
15 C. Deviannapoorani, L. S. Shankar, S. Ramakumar and R. Murugan, *Ionics*, 2016, **22**, 1281–1289.
16 Y. Li, J.-T. Han, C.-A. Wang, H. Xie and J. B. Goodenough, *J. Mater. Chem.*, 2012, **22**, 15357–15361.
17 S. Ohta, T. Kobayashi and T. Asaoka, *J. Power Sources*, 2011, **196**, 3342–3345.
18 J. Awaka, N. Kijima, H. Hayakawa and J. Akimoto, *J. Solid State Chem.*, 2009, **182**, 2046–2052.
19 C. Ma, Y. Cheng, K. Yin, J. Luo, A. Sharafi, J. Sakamoto, J. Li, K. L. More, N. J. Dudney and M. Chi, *Nano Lett.*, 2016, **16**, 7030–7036.
20 A. Sharafi, H. M. Meyer, J. Nanda, J. Wolfenstine and J. Sakamoto, *J. Power Sources*, 2016, **302**, 135–139.
21 D. Rettenwander, R. Wagner, A. Reyer, M. Bonta, L. Cheng, M. M. Doeff, A. Limbeck, M. Wilkening and G. Amthauer, *J. Phys. Chem. C*, 2018, **122**, 3780–3785.
22 Y. Shimonishi, A. Toda, T. Zhang, A. Hirano, N. Imanishi, O. Yamamoto and Y. Takeda, *Solid State Ionics*, 2011, **183**, 48–53.
23 E. Rangasamy, J. Wolfenstine and J. Sakamoto, *Solid State Ionics*, 2012, **206**, 28–32.
24 J. Košir, S. Mousavihashemi, B. P. Wilson, E.-L. Rautama and T. Kallio, *Solid State Ionics*, 2022, **380**, 115943.
25 M. Saccoccio, J. Yu, Z. Lu, S. C. Kwok, J. Wang, K. K. Yeung, M. M. Yuen and F. Ciucci, *J. Power Sources*, 2017, **365**, 43–52.
26 J. Tan and A. Tiwari, *ECS Solid State Lett.*, 2012, **1**, Q57–Q60.
27 S. Yu and D. J. Siegel, *Chem. Mater.*, 2017, **29**, 9639–9647.
28 T. W. Heo, A. Grieder, B. Wang, M. Wood, T. Hsu, S. A. Akhade, L. F. Wan, L.-Q. Chen, N. Adelstein and B. C. Wood, *npj Comput. Mater.*, 2021, **7**, 214.
29 J. A. Dawson, P. Canepa, T. Famprikis, C. Masquelier and M. S. Islam, *J. Am. Chem. Soc.*, 2018, **140**, 362–368.
30 K. Kawahara, R. Ishikawa, K. Nakayama, T. Higashi, T. Kimura, Y. H. Ikuhara, N. Shibata and Y. Ikuhara, *J. Power Sources*, 2019, **441**, 227187.
31 N. Bernstein, M. D. Johannes and K. Hoang, *Phys. Rev. Lett.*, 2012, **109**, 205702.
32 H. Xie, J. A. Alonso, Y. Li, M. T. Fernández-Díaz and J. B. Goodenough, *Chem. Mater.*, 2011, **23**, 3587–3589.
33 R. Jalem, Y. Yamamoto, H. Shiiba, M. Nakayama, H. Munakata, T. Kasuga and K. Kanamura, *Chem. Mater.*, 2013, **25**, 425–430.
34 D. Rettenwander, P. Blaha, R. Laskowski, K. Schwarz, P. Bottke, M. Wilkening, C. A. Geiger and G. Amthauer, *Chem. Mater.*, 2014, **26**, 2617–2623.
35 B. Karasulu, S. P. Emge, M. F. Groh, C. P. Grey and A. J. Morris, *J. Am. Chem. Soc.*, 2020, **142**, 3132–3148.
36 H. Buschmann, J. Dölle, S. Berendts, A. Kuhn, P. Bottke, M. Wilkening, P. Heitjans, A. Senyshyn, H. Ehrenberg, A. Lotnyk, V. Duppel, L. Kienle and J. Janek, *Phys. Chem. Chem. Phys.*, 2011, **13**, 19378–19392.
37 M. A. Howard, O. Clemens, E. Kendrick, K. S. Knight, D. C. Apperley, P. A. Anderson and P. R. Slater, *Dalton Trans.*, 2012, **41**, 12048–12053.
38 C. Bernuy-Lopez, W. Manalastas, J. M. Lopez del Amo, A. Aguadero, F. Aguesse and J. A. Kilner, *Chem. Mater.*, 2014, **26**, 3610–3617.
39 D. Rettenwander, J. Langer, W. Schmidt, C. Arrer, K. J. Harris, V. Terskikh, G. R. Goward, M. Wilkening and G. Amthauer, *Chem. Mater.*, 2015, **27**, 3135–3142.
40 A. Düvel, A. Kuhn, L. Robben, M. Wilkening and P. Heitjans, *J. Phys. Chem. C*, 2012, **116**, 15192–15202.
41 Z. Hu, H. Liu, H. Ruan, R. Hu, Y. Su and L. Zhang, *Ceram. Int.*, 2016, **42**, 12156–12160.
42 Y. Jin and P. J. McGinn, *J. Power Sources*, 2011, **196**, 8683–8687.
43 J. Sastre, A. Priebe, M. Döbeli, J. Michler, A. N. Tiwari and Y. E. Romanyuk, *Adv. Mater. Interfaces*, 2020, **7**, 2000425.

44 R. Wagner, G. J. Redhammer, D. Rettenwander, A. Senyshyn, W. Schmidt, M. Wilkening and G. Amthauer, *Chem. Mater.*, 2016, **28**, 1861–1871.
45 S. Lobe, A. Bauer, D. Sebold, N. Wettengl, D. Fattakhova-Rohlfing and S. Uhlenbruck, *Open Ceram.*, 2022, **10**, 100268.
46 H. El Shinawi and J. Janek, *J. Power Sources*, 2013, **225**, 13–19.
47 K. Ishiguro, Y. Nakata, M. Matsui, I. Uechi, Y. Takeda, O. Yamamoto and N. Imanishi, *J. Electrochem. Soc.*, 2013, **160**, A1690–A1693.
48 X. Zhang, T.-S. Oh and J. W. Fergus, *J. Electrochem. Soc.*, 2019, **166**, A3753–A3759.
49 L. J. Miara, W. D. Richards, Y. E. Wang and G. Ceder, *Chem. Mater.*, 2015, **27**, 4040–4047.
50 L. Dhivya and R. Murugan, *ACS Appl. Mater. Interfaces*, 2014, **6**, 17606–17615.
51 M. Kotobuki and M. Koishi, *J. Alloys Compd.*, 2020, **826**, 154213.
52 J. Gai, E. Zhao, F. Ma, D. Sun, X. Ma, Y. Jin, Q. Wu and Y. Cui, *J. Eur. Ceram. Soc.*, 2018, **38**, 1673–1678.
53 B. Liu, J. Yang, H. Yang, C. Ye, Y. Mao, J. Wang, S. Shi, J. Yang and W. Zhang, *J. Mater. Chem. A*, 2019, **7**, 19961–19969.
54 G. Kresse and J. Hafner, *Phys. Rev. B: Condens. Matter Mater. Phys.*, 1993, **47**, 558–561.
55 G. Kresse and J. Furthmüller, *Comput. Mater. Sci.*, 1996, **6**, 15–50.
56 G. Kresse and J. Furthmüller, *Phys. Rev. B: Condens. Matter Mater. Phys.*, 1996, **54**, 11169–11186.
57 J. P. Perdew, A. Ruzsinszky, G. I. Csonka, O. A. Vydrov, G. E. Scuseria, L. A. Constantin, X. Zhou and K. Burke, *Phys. Rev. Lett.*, 2008, **100**, 136406.
58 A. V. Krukau, O. A. Vydrov, A. F. Izmaylov and G. E. Scuseria, *J. Chem. Phys.*, 2006, **125**, 224106.
59 B. A. D. Williamson, J. Buckeridge, N. P. Chadwick, S. Sathasivam, C. J. Carmalt, I. P. Parkin and D. O. Scanlon, *Chem. Mater.*, 2019, **31**, 2577–2589.
60 P. Deák, B. Aradi, T. Frauenheim, E. Janzén and A. Gali, *Phys. Rev. B: Condens. Matter Mater. Phys.*, 2010, **81**, 153203.
61 B. A. D. Williamson, G. J. Limburn, G. W. Watson, G. Hyett and D. O. Scanlon, *Matter*, 2020, **3**, 759–781.
62 G. Kresse and D. Joubert, *Phys. Rev. B: Condens. Matter Mater. Phys.*, 1999, **59**, 1758–1775.
63 J. Shen nwinner, J. Riebesell and J. Zeng, *materialsproject/pymatgen-analysis-defects: v2023.02.07*, 2023.
64 C. Freysoldt, B. Grabowski, T. Hickel, J. Neugebauer, G. Kresse, A. Janotti and C. G. Van de Walle, *Rev. Mod. Phys.*, 2014, **86**, 253–305.
65 S. Lany and A. Zunger, *Phys. Rev. B: Condens. Matter Mater. Phys.*, 2008, **78**, 235104.
66 S. T. Murphy and N. D. M. Hine, *Phys. Rev. B: Condens. Matter Mater. Phys.*, 2013, **87**, 094111.
67 J. Buckeridge, D. Scanlon, A. Walsh and C. Catlow, *Comput. Phys. Commun.*, 2014, **185**, 330–338.
68 M. Kotobuki, K. Kanamura, Y. Sato, K. Yamamoto and T. Yoshida, *J. Power Sources*, 2012, **199**, 346–349.
69 M. W. Chase Jr, *NIST-JANAF Thermochemical Tables*, American Chemical Society, American Institute of Physics for the National Institute of Standards and Technology, Washington, DC, New York, 4th edn, 1998.
70 K. Reuter and M. Scheffler, *Phys. Rev. B: Condens. Matter Mater. Phys.*, 2001, **65**, 035406.
71 J. Buckeridge, *Comput. Phys. Commun.*, 2019, **244**, 329–342.
72 K. Momma and F. Izumi, *J. Appl. Crystallogr.*, 2011, **44**, 1272–1276.
73 K. Kataoka and J. Akimoto, *Solid State Ionics*, 2020, **349**, 115312.
74 T. Kimura, Y. Yamada, K. Yamamoto, T. Matsuda, H. Nomura and T. Hirayama, *J. Am. Ceram. Soc.*, 2017, **100**, 1313–1319.
75 K. Ajith, P. Christopher Selvin, K. Abhilash, P. Sivaraj, B. Nalini and G. Soundarya, *Mater. Today: Proc.*, 2022, **50**, 2836–2839.
76 A. G. Squires, D. O. Scanlon and B. J. Morgan, *Chem. Mater.*, 2020, **32**, 1876–1886.
77 P. Borlido, J. Schmidt, A. W. Huran, F. Tran, M. A. L. Marques and S. Botti, *npj Comput. Mater.*, 2020, **6**, 96.
78 J. P. Perdew and A. Zunger, *Phys. Rev. B: Condens. Matter Mater. Phys.*, 1981, **23**, 5048–5079.
79 F. Han, A. S. Westover, J. Yue, X. Fan, F. Wang, M. Chi, D. N. Leonard, N. J. Dudney, H. Wang and C. Wang, *Nat. Energy*, 2019, **4**, 187–196.
80 F. Aguesse, W. Manalastas, L. Buannic, J. M. Lopez del Amo, G. Singh, A. Llordés and J. Kilner, *ACS Appl. Mater. Interfaces*, 2017, **9**, 3808–3816.
81 Y. Song, L. Yang, W. Zhao, Z. Wang, Y. Zhao, Z. Wang, Q. Zhao, H. Liu and F. Pan, *Adv. Energy Mater.*, 2019, **9**, 1900671.
82 A. G. Squires, D. W. Davies, S. Kim, D. O. Scanlon, A. Walsh and B. J. Morgan, *Phys. Rev. Mater.*, 2022, **6**, 085401.
83 T. Grande, J. R. Tolchard and S. M. Selbach, *Chem. Mater.*, 2012, **24**, 338–345.
84 J. Maier, *Phys. Chem. Chem. Phys.*, 2003, **5**, 2164–2173.
85 U. Aschauer, R. Pfenninger, S. M. Selbach, T. Grande and N. A. Spaldin, *Phys. Rev. B: Condens. Matter Mater. Phys.*, 2013, **88**, 054111.
86 C. Schwab, G. Häuschen, M. Mann, C. Roitzheim, O. Guillon, D. Fattakhova-Rohlfing and M. Finsterbusch, *J. Mater. Chem. A*, 2023, **11**, 5670–5680.
87 A. Navrotsky and O. Kleppa, *J. Inorg. Nucl. Chem.*, 1967, **29**, 2701–2714.
88 H. S. C. O'Neill and A. Navrotsky, *Am. Mineral.*, 1983, **68**, 181–194.
89 K. Greenwood, D. Ko, D. Vander Griend, G. Sarjeant, J. Milgram, E. Garrity, D. DeLoach, K. Poeppetmeier, P. Salvador and T. Mason, *Inorg. Chem.*, 2000, **39**, 3386–3391.
90 G. H. Olsen, S. M. Selbach and T. Grande, *Phys. Chem. Chem. Phys.*, 2015, **17**, 30343–30351.
91 J. Allen, J. Wolfenstine, E. Rangasamy and J. Sakamoto, *J. Power Sources*, 2012, **206**, 315–319.
92 F. A. García Daza, M. R. Bonilla, A. Llordés, J. Carrasco and E. Akhmatskaya, *ACS Appl. Mater. Interfaces*, 2019, **11**, 753–765.

93 P. Posch, S. Lunghammer, S. Berendts, S. Ganschow, G. J. Redhammer, A. Wilkening, M. Lerch, B. Gadermaier, D. Rettenwander and H. M. R. Wilkening, *Energy Storage Mater.*, 2020, **24**, 220–228.
94 P. Bottke, D. Rettenwander, W. Schmidt, G. Amthauer and M. Wilkening, *Chem. Mater.*, 2015, **27**, 6571–6582.
95 B. Stanje, D. Rettenwander, S. Breuer, M. Uitz, S. Berendts, M. Lerch, R. Uecker, G. Redhammer, I. Hanzu and M. Wilkening, *Ann. Phys.*, 2017, **529**, 1700140.